ACS APPLIED MATERIALS & INTERFACES

Research Article

www.acsami.org

Cluster Beam Deposition of $Cu_{2-X}S$ Nanoparticles into Organic Thin Films

Michael W. Majeski, Igor L. Bolotin, and Luke Hanley*

Department of Chemistry (MC 111), University of Illinois at Chicago, Chicago, Illinois 60607, United States

Supporting Information

ABSTRACT: Bulk-heterojunction films composed of semiconductor nanoparticles blended with organic oligomers are of interest for photovoltaic and other applications. $Cu_{2-X}S$ nanoparticles were cluster beam deposited into thermally evaporated pentacene or quaterthiophene to create bulk-heterojunction thin films. The nanoparticle stoichiometry, morphology, and chemistry within these all-gas phase deposited films were characterized by X-ray photoelectron spectroscopy (XPS) and electron microscopy. $Cu_{2-X}S$ nanoparticles were (at most) only slightly copper-deficient with respect to Cu_2S; ~2.5 nm diameter, unoxidized $Cu_{2-X}S$ nanoparticles formed in both pentacene and quaterthiophene, as the matrix was not observed to impact the nanoparticle morphology or chemical structure. Cluster beam deposition allowed direct control of the nanoparticle stoichiometry and nanoparticle:organic ratio. Chemical states or Wagner plots were combined with other XPS data analysis strategies to determine the metal oxidation state, indicating that Cu(I) was predominant over Cu(II) in the $Cu_{2-X}S$ nanoparticles.

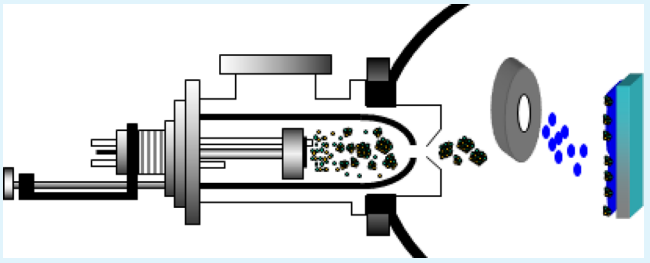

KEYWORDS: *sputtering, copper sulfide, photovoltaic, pentacene, quaterthiophene*

I. INTRODUCTION

Earth abundant and nontoxic materials possess economic and environmental advantages for use in photovoltaic devices.[1] The goal of low-cost and efficient materials for solar energy conversion has motivated investigations of nanostructured materials for photovoltaic technologies.[2−4] Hybrid organic−inorganic materials make up one class of nanostructured materials considered for use in bulk-heterojunction devices because of their low cost and potential ease of large-scale fabrication. Copper-based chalcogenide nanoparticles, whose 1.1−1.7 eV bandgaps can be size-tuned via quantum confinement, are one of several nanoparticle-based candidates for use in photovoltaics.[5−8] Copper sulfide nanoparticles are also potentially useful for photodetectors, nanoscale electric switches, biosensors, and batteries.[9,10] However, the stability of copper sulfide in air has been a long-standing barrier to the use of this otherwise promising solar energy absorber, as oxidation leads to substoichiometric phases and gives rise to excessive p-doping.[11,12] Even without oxidation, copper sulfide nanoparticles can form up to five different stoichiometries or phases,[13] hence the use here of the $Cu_{2-X}S$ notation.

Over the past decade, the efficiency of bulk-heterojunction-based organic photovoltaic devices has quadrupled.[14] Bulk-heterojunction devices are constructed using materials consisting of a donor and an acceptor: the donor can be a conducting polymer or organic oligomer that absorbs optically and generates excitons, while the acceptor can be an inorganic nanocrystal that, while also absorbing radiation, can additionally facilitate electron transfer.[15] The nanocomposite films prepared here are based on design rules for bulk-heterojunction films driven by the choice of $Cu_{2-X}S$ nanoparticles as the inorganic phase and the overlap of their highest occupied and lowest unoccupied molecular orbitals with those of an adjacent organic oligomer.[14,16] Pentacene and another organic semiconducting oligomer, quaterthiophene, are used in prototype photovoltaic devices for their high carrier mobility and stability with respect to oxidation.[17−20]

This paper describes the preparation of $Cu_{2-X}S$ nanoparticles by cluster beam deposition.[21] Previous work depositing PbS nanoparticles showed that cluster beam deposition allows direct control of nanoparticle properties such as surface chemistry without the need for ligand capping.[22,23] $Cu_{2-X}S$ nanoparticles were deposited into thermally evaporated pentacene or quaterthiophene to create a bulk-heterojunction thin film. These all-gas phase deposited films were characterized by X-ray photoelectron spectroscopy (XPS) and electron microscopy. Chemical states or Wagner plots were combined with other XPS analysis strategies to distinguish the oxidation state of copper.

II. EXPERIMENTAL SECTION

A. Deposition of $Cu_{2-X}S$ Nanoparticles, Organic Oligomer, and Carbonaceous Film. $Cu_{2-X}S$ nanoparticles were generated from a copper target inside the cluster beam deposition source (Nanogen-

Received: May 9, 2014
Accepted: June 30, 2014
Published: June 30, 2014

   dx.doi.org/10.1021/am5028428 | ACS Appl. Mater. Interfaces 2014, 6, 12901−12908

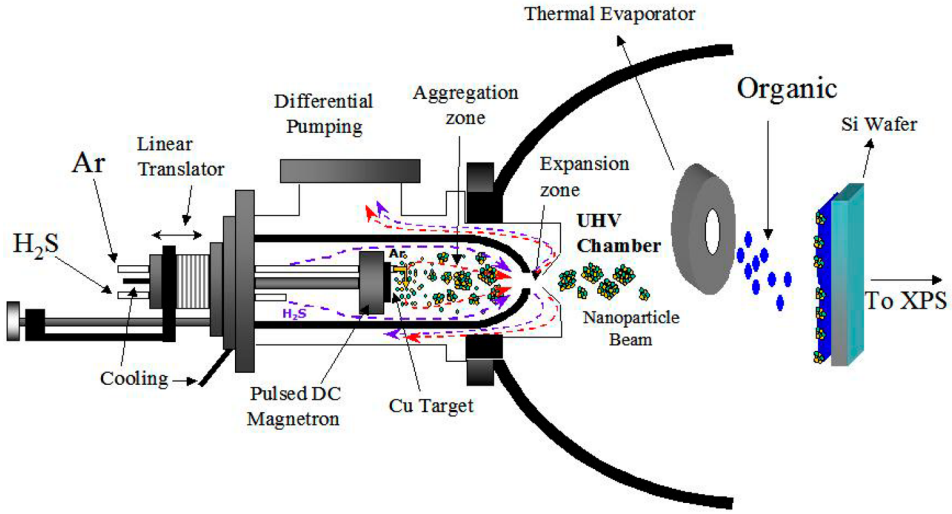

Figure 1. Cross section of the pulsed DC magnetron cluster source for cluster beam deposition. The evaporator for organic deposition and the target are also shown.

50, Mantis Deposition Ltd., Oxfordshire, U.K.) shown in Figure 1 by pulsed DC magnetron sputtering with Ar and reactive hydrogen sulfide (H_2S) gas.[22] The magnetron was housed in a water-cooled gas aggregation source with a base pressure of 10^{-8} Torr, an operating pressure near 30 mTorr, and an operating power of ∼75 W, in which $Cu_{2-X}S$ clusters were allowed to form by reactive sputtering and nucleation for subsequent deposition onto a silicon substrate. Silicon wafers [n-type Si(100) wafers, Atomergic Chemical Corp., Melville, NY] were used as substrates for deposition after hydrogen termination by HF etching.

A significant effort was undertaken to develop conditions for pulsed magnetron sputtering of stoichiometric copper sulfide. Sputtering occurs within the magnetron after the striking voltage is applied to the copper target cathode, the Ar sputtering gas undergoes ionization, a glow discharge is ignited, and Ar ions begin to sputter the target. The magnetron configuration was comprised of an unbalanced planar magnetron with a circular target disk and a set of unbalanced permanent magnets placed directly behind the target to create an electron bottle. $Cu_{2-X}S$ nanoparticles were formed by adding H_2S gas to the discharge, but H_2S complicates the process[24] by decreasing the deposition rate (see the Supporting Information) and discharge stability. For example, arcing in the discharge can occur, which degrades the quality of the deposited film, gives rise to the presence of particulates and pinholes, damages the target by local melting, and can eventually damage the discharge power supply.[25] Incorporation of a pulsing unit (Sparc-le V, Advanced Energy, Fort Collins, CO) during magnetron sputtering of copper sulfide was implemented to prevent arcing, target damage, and other deleterious effects. Pulsing the DC discharge power at 20 kHz was found here to stabilize process parameters with an absence of arcing and was previously shown to improve the quality of the deposited films.[25]

The gaseous $Cu_{2-X}S$ clusters were deposited both simultaneously and in a stepwise manner onto the Si substrate with pentacene (P0030, already purified by sublimation, TCI of America, Portland, OR) evaporated from a heated ceramic crucible (LTE 11000K, 1 cm^3, K. J. Lesker, Pittsburgh, PA). Pentacene was deposited at a rate of 15−20 Å/min to achieve a ∼100 nm thick film by thermal evaporation at 160−190 °C (depending on the amount of organic remaining in the crucible). Pentacene was deposited at a rate 10−15 times higher than that of the nanoparticles, as measured with a quartz crystal microbalance (see below). Quaterthiophene was deposited at a similar rate of 15 Å/min in attempts to achieve the same film thickness by evaporating in the range of 140−240 °C.

Acetylene ions with a kinetic energy of 50 eV were generated by a Kaufman ion source (IBS 250, 3 cm, Veeco/Commonwealth Scientific, Plainview, NY) and used to deposit a thin carbonaceous film atop the silicon wafer (termed C/Si) to allow investigation of nanoparticle stoichiometry free from effects of pentacene or quaterthiophene.[23,26]

B. X-ray Photoelectron Spectroscopy. Samples were characterized by high-resolution monochromatic X-ray photoelectron spectroscopy (XPS), using a previously described instrument.[27] A monochromatic 1486 eV Al Kα X-ray source was operated at 300 W (15 keV and 20 mA emission current). Semiquantitative analysis was also confirmed using a commercial instrument (Kratos AXIS-165 Surface Analysis System) that also operated at high resolution with a monochromatic Al Kα X-ray source, which utilized a charge neutralization coil (data not shown).

After the deposition of films, samples were transferred in vacuum for analysis by XPS, preventing any exposure to the atmosphere. This was accomplished by joining together the CBD instrument and XPS chamber with an interconnecting high-vacuum load lock (see the Supporting Information). Maintaining the films under vacuum en route to analysis prevented oxidation, as verified by XPS.

All XPS binding energies were charge corrected and referenced to the C 1s peak for aliphatic carbon at 285.0 eV. Both S 2p and Cu 2p core levels displayed contributions from the 3/2 and 1/2 degenerate spin orbit peaks whose area ratios were 2:1. The S 2p spin orbit splitting was taken as 1.20 eV (determined experimentally vs the literature average of 1.17 eV[28]), while a 19.8 eV splitting was used for Cu 2p (vs the NIST value of 19.9 eV). Binding energies refer to those for the S $2p_{3/2}$ and Cu $2p_{3/2}$ spin orbit peaks only, unless explicitly noted otherwise. The elemental content was analyzed from averages of at least three spectra using only the $2p_{3/2}$ spin orbit component from the core level spectra.

C. Quartz Crystal Microbalance and Electron Microscopy. A quartz crystal microbalance (SQC-222, Sigma Instruments, Fort Collins, CO) was used to monitor the deposition of both nanoparticles and the organic matrix.

Transmission electron microscopy (TEM) was performed using a field-emission electron microscope (JEOL 3010F, JEOL, Peabody, MA) with an acceleration voltage of 200 keV. Nanoparticles were codeposited with an organic matrix directly onto a 200 mesh carbon-coated copper grid to allow imaging. High-angle annular dark field imaging scanning transmission electron microscopy (HAADF-STEM) was performed using a probe aberration-corrected 200 keV STEM/TEM with a cold field emission source with 0.35 eV energy resolution (JEM-ARM200CF, JEOL) and demonstrated resolution of 0.08 nm for HAADF imaging at 200 keV.[29]

III. RESULTS AND DISCUSSION

A. Copper:Sulfur Stoichiometry and Deposition Rate. Figure 2 shows the XPS survey scan of $Cu_{2-X}S$ nanoparticles

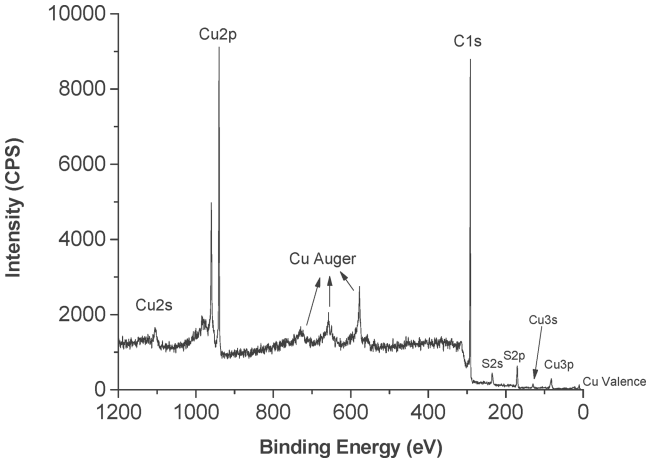

Figure 2. Survey X-ray photoelectron spectrum (XPS) of the $Cu_{2-X}S$ cluster beam deposited onto the Si wafer coated with an ~100 nm thick film of thermally evaporated pentacene.

deposited on a silicon wafer that was previously deposited for 1 h with the organic semiconductor pentacene. The Cu $2p_{3/2}$ and S $2p_{3/2}$ peaks were used to analyze the sample stoichiometry. The absence of a silicon signal in the XPS survey scan indicated complete coverage of the substrate by pentacene and nanoparticles. The high sulfur content and the absence of an oxygen signal in the XPS survey scan indicated the sole presence of copper sulfide.

$Cu_{2-X}S$ nanoparticles were also examined without deposited pentacene to better determine their stoichiometry and to evaluate the Cu oxidation state via comparison with literature photoelectron peak binding energies (see the Supporting Information for XPS survey scans similar to that shown in Figure 2). $Cu_{2-X}S$ nanoparticles were deposited onto a thin carbonaceous film on the Si substrate (denoted C/Si) previously prepared by 50 eV acetylene ion deposition, as described previously.[23,26] It was assumed that the nanoparticles coalesced into films in the absence of pentacene or another organic matrix, although the film morphology was not confirmed by electron microscopy.

Nanoparticles were deposited under a variety of flow rate ratios of sputtering gas (Ar) to reactive gas (H_2S), after which the stoichiometries of the resultant films were examined by XPS. The results shown in Table 1 indicate that even slight changes in the Ar:H_2S ratio were found to affect the chemical composition of the deposited film. The rate of deposition of pure Cu with only argon flow was maximal at 0.8 sccm (standard cubic centimeters) of argon and declined as the flow rate was increased. A flow with a 1:1 ratio produced ~82 atom % Cu content in copper rich films. Films produced at a 2:2 ratio indicated an average chemical composition of 66 ± 1 atom % copper and 34 ± 1 atom % sulfur, nominally corresponding to Cu_2S. All nanoparticles were subsequently deposited at a 2:2 ratio but are labeled as $Cu_{2-X}S$ to represent the potential existence of multiple copper sulfide phases with stoichiometries close to both chalcocite (Cu_2S) and djurleite ($Cu_{1.94}S$) (see below). Several phases are known to coexist with chalcocite, which is dominant in the bulk.[13]

Table 1. Summary of Films of $Cu_{2-X}S$ Prepared at Different Flow Ratios of Sputtering (Ar) and Reactive (H_2S) Gas Given in Standard Cubic Centimeters (sccm)[a]

ratio	Ar flow (sccm)	H_2S flow (sccm)	% Cu	% S
1:1	1.00	1.00	82 ± 8	18 ± 8
1:2	1.00	2.00	78 ± 7	22 ± 7
1:3	1.00	3.00	71 ± 2	29 ± 2
2:2	2.00	2.00	66 ± 1	34 ± 1

[a]Cu and S elemental percentages were determined from XPS peak areas, while the deposition rate was measured with a quartz crystal microbalance.

Sputtering of the Cu target was inhibited slightly by increasing partial pressures of H_2S gas, an effect related to the well-known hysteresis in reactive sputtering processes.[30] However, the deposition rate as measured by the quartz crystal microbalance (see the Supporting Information) varied only slightly for different sputtering:reactive gas ratios. Thus, only an average deposition rate of 2.4 ± 0.2 Å/min across all gas flow ratios is reported here, based on an assumed copper sulfide density of 5.68 g/cm^2.

B. Electron Microscopy. $Cu_{2-X}S$ that was cluster beam deposited into either organic matrix was found by electron microscopy to maintain a distinct nanoparticle morphology. TEM micrographs (shown in the Supporting Information) show films consisting of a blended bulk heterojunction of $Cu_{2-X}S$ nanoparticles embedded in quaterthiophene or pentacene. The presence of spherical particles was evident in TEM micrographs of samples prepared with a relatively low deposition rate of organic on holey carbon copper mesh grids but were difficult to distinguish because of poor phase contrast (see the Supporting Information).

Imaging with high-angle annular dark field scanning transmission electron microscopy (HAADF-STEM) based on atomic Z contrast was therefore used to confirm the presence of nanoparticles. The HAADF-STEM images in Figure 3 confirm that nanoparticles observed in TEM were monodispersed $Cu_{2-X}S$ nanoparticles. For the dark field imaging shown in Figure 3, the black part of the image represents the absence of any signal arising from interference of the electron beam with the sample and shows the gaps in the copper grid. The dark gray parts of the images represent pentacene or quaterthiophene supported on holey carbon, while the lighter gray spheres represent the $Cu_{2-X}S$ nanoparticles. A poorer phase contrast was observed for HAADF-STEM of the pentacene versus quaterthiophene films, so the latter were used to determine nanoparticle size distributions. An average diameter of 2.3 ± 0.4 nm was measured from statistical averaging of more than 300 individual $Cu_{2-X}S$ nanoparticles in quaterthiophene, with the histogram shown in Figure 3c generated using images similar to Figure 3b. Comparison of panels a and b of Figure 3 and indicates similar nanoparticle sizes appear in both pentacene and quaterthiophene. Nanoparticle features were absent from films with little or no copper sulfide.

C. Copper Chemical State for $Cu_{2-X}S$ Nanoparticles in Pentacene. The following results apply to only $Cu_{2-X}S$ nanoparticles embedded in organic pentacene, unless explicitly noted otherwise. Figure 4a shows the Cu 2p core level XP spectrum of $Cu_{2-X}S$ nanoparticles in pentacene without any air exposure, whose experimental binding energy was 933.1 ± 0.5 eV. This Cu 2p binding energy agreed well with the average values for monovalent copper sulfide, Cu_2S, from the NIST XPS database[28] of 932.5 ± 0.3 eV. Nevertheless, the binding energy overlap present in copper and other first row transition metals can complicate spectral interpretation because of the

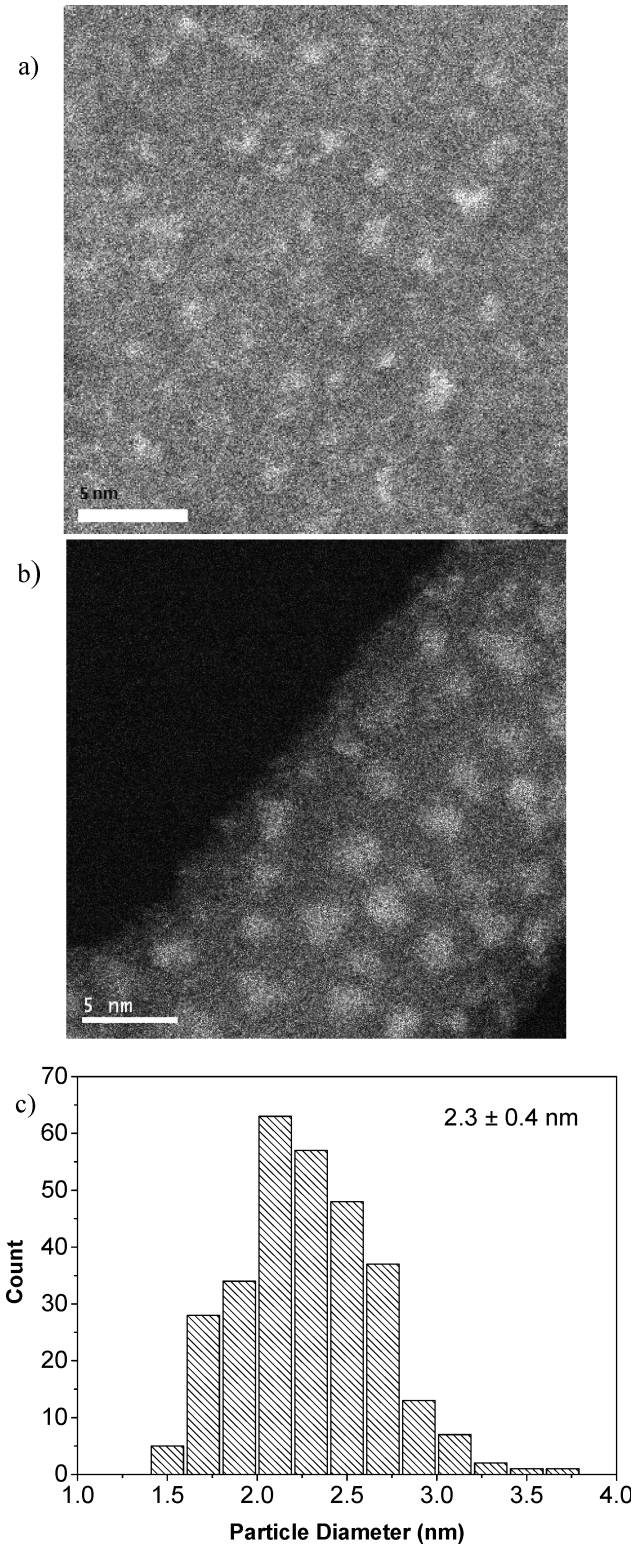

Figure 3. HAADF-STEM images of $Cu_{2-X}S$ nanoparticles in (a) pentacene and (b) quaterthiophene. (c) Histogram of the diameter of $Cu_{2-X}S$ nanoparticles in quaterthiophene.

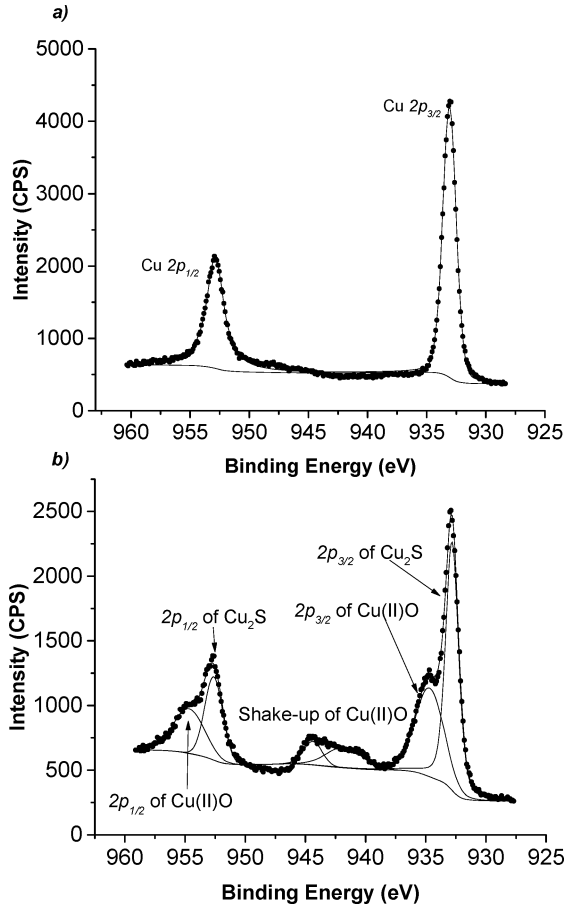

Figure 4. (a) XPS core level spectra of Cu 2p for $Cu_{2-X}S$ nanoparticles deposited atop a thin film of pentacene without any atmospheric exposure. (b) Cu 2p region after exposure to the atmosphere for several days, for nanoparticles deposited without pentacene. Points are raw data, and lines are fits to the data, with background subtractions shown.

complexity of their respective 2p spectra. Table 2 lists published photoelectron binding energies for different oxidation states of copper,[31] updated here to include more recent references from the NIST database.

The 932.6 eV accepted value for the copper metal binding energy, Cu(0), suggested a slightly higher oxidation state present here as all experimental values lay above this value at 933.1 ± 0.5 eV. Furthermore, the absence of a Cu $2p_{3/2}$ component well above 933.0 eV is a common indicator of the presence of only Cu(I).[32] Figure 4b presents the analysis of the Cu 2p region after exposure of nanoparticles deposited in the absence of a protective pentacene overlayer to the atmosphere for several days. The evidence of this oxidation can be observed in the Cu 2p spectra, where the presence of additional p peaks was seen in the $Cu_{2-X}S$/C/Si air-oxidized film, shown in Figure 4b near 935 eV for Cu $2p_{3/2}$ (as well as a peak at 955 eV for Cu $2p_{1/2}$). Figure 4 clearly displays the oxidation of Cu(I) to Cu(II) and the presence of copper oxide (see below). By contrast, unoxidized $Cu_{2-X}S$ displayed only the single Cu $2p_{3/2}$ component displayed in Figure 4a.

Nevertheless, distinguishing Cu(I) from Cu(II) in sulfur-containing compounds on the basis of photoelectron peak binding energies alone was limited by the observation that Cu $2p_{3/2}$ appeared at ~932.5 eV in both cases.[28] Further support for the sole presence of Cu(I) in unoxidized copper sulfide is found in the absence of excited state or shake-up satellites in the Cu 2p spectra.[31,33] Figure 4b shows the appearance of the shake-up satellites in the region from 940 to 945 eV upon oxidation of a fraction of Cu(I) to Cu(II), as noted above.[32] The shake-up features present in Cu 2p spectra were

Table 2. Comparison of Experimental XPS Data on $Cu_{2-X}S$ Deposited on a Carbonaceous (C/Si) or Pentacene Film with Literature Values[28] for Different Copper Compounds in Various Oxidation States[a]

	Cu $2p_{3/2}$ binding energy (eV)	Cu Auger kinetic energy $L_3M_{45}M_{45}$ (eV)	modified Auger parameter (eV)[b]	S $2p_{3/2}$ binding energy (eV)[c]
literature compound				
Cu(0)	932.6 ± 0.2 (29)	918.6 ± 0.2 (25)	1851.2 ± 0.3	–
$Cu(I)_2O$	932.4 ± 0.2 (20)	916.7 ± 0.3 (12)	1849.1 ± 0.4	–
Cu(II)O	933.7 ± 0.4 (27)	917.9 ± 0.2 (12)	1851.6 ± 0.4	–
$Cu(I)_2S$	932.5 ± 0.3 (10)	917.1 ± 0.2 (6)	1849.6 ± 0.4	162.3 ± 1.7 (12)
Cu(II)S	932.5 ± 1.0 (9)	918.1 ± 0.2 (6)	1850.6 ± 1.0	162.1 ± 0.6 (5)
experimental $Cu_{2-X}S$				
C/Si, no air exposure	933.0 ± 0.1	915.8 ± 0.0	1848.8 ± 0.1	162.1 ± 0.1
C/Si, oxidized	935.6 ± 1.1	914.9 ± 0.5	1850.5 ± 1.2	163.6 ± 0.4
in pentacene	933.1 ± 0.5	915.7 ± 0.1	1848.8 ± 0.5	162.4 ± 0.2

[a]Numbers of literature values from the database are given in parentheses. See the text for an explanation. [b]$\alpha' = E_k(C'C''C''') + E_b(C)$, as discussed in the text. See eq 1. [c]Core component.

undisputed evidence of an open $3d^9$ shell of Cu(II)[34] arising from copper oxide and were fit with two components.[35]

XPS peak shifts alone can be insufficient to reveal surface chemical states, especially for metal sulfide compounds, but Auger peaks are sometimes more sensitive to oxidation state. The Cu $L_3M_{45}M_{45}$ Auger line position corroborated the presence of Cu(I) in the pristine, unexposed films, which appeared at a kinetic energy of 915.7 eV (see the Supporting Information). The relatively wide gap between the Auger line positions for Cu(0) at 918.6 ± 0.2 eV and those for Cu(I) compounds Cu_2O and Cu_2S at 916.7 and 917.1 eV, respectively, also supported the assignment of the $Cu_{2-X}S$ nanoparticles in pentacene to Cu(I) given their 915.8 eV Auger peak.[36,37] The Cu(II) compounds CuO and CuS also appear around 918 eV, showing the larger peak position differences between oxidation states for Auger data compared to photoelectron peaks for this transition metal, corresponding to Cu(I).

A plot of the kinetic energy of the Auger Cu $L_3M_{45}M_{45}$ line versus the Cu $2p_{3/2}$ peak photoelectron binding energy can provide yet more information regarding the copper oxidation state. Prior work has shown that such Wagner or chemical state plots can help distinguish different chemical states of core-ionized atoms.[33,38] Wagner plots define a modified Auger parameter α', which is the sum of the photoelectron peak binding energy and the Auger peak kinetic energy, and collectively provide chemical state information free of charge corrections and work function measurement:

$$\alpha' = \alpha + h\nu = E_k(C'C''C''') + E_b(C) \quad (1)$$

where α is the electronic polarizability of a chemical species, $E_k(C'C''C''')$ is the kinetic energy of an X-ray-excited Auger electron (commonly from a core−core−core Auger decay process), and $E_b(C)$ is the binding energy for the core ionized species. It has been argued that a nonlocal screening mechanism is evident for Cu(I) compounds during the Auger emission process, and therefore, the simple electrostatic model can be applied when calculating the Auger parameter shifts.[33] Application of these concepts allows use of the Auger parameter shifts in semiconductors to characterize the local environment of core-ionized atoms.[33] The diagonal lines on the Wagner plot represent a constant α', and thus, values appearing on the same line with a unit slope have the same modified Auger parameter (when the photoelectron peak binding energy is plotted as decreasing along the x-axis). Compounds appearing on the same line are thought to be undergoing similar initial state effects.[33]

Figure 5 shows the Wagner plot constructed from compounds with different Cu chemical states listed in the NIST database[28] (error bars represent the standard deviation of averaged database values). There are distinct areas in the graph for Cu(0), Cu(I), and Cu(II) compounds.[37,39,40] The experimental results for $Cu_{2-X}S$ nanoparticles fell within 1.1 eV in either coordinate of Cu_2S and within the area where all Cu(I) compounds appear. The Wagner plot is further evidence that Cu(I) is the predominant oxidation state present in the deposited nanoparticles prior to any air exposure.

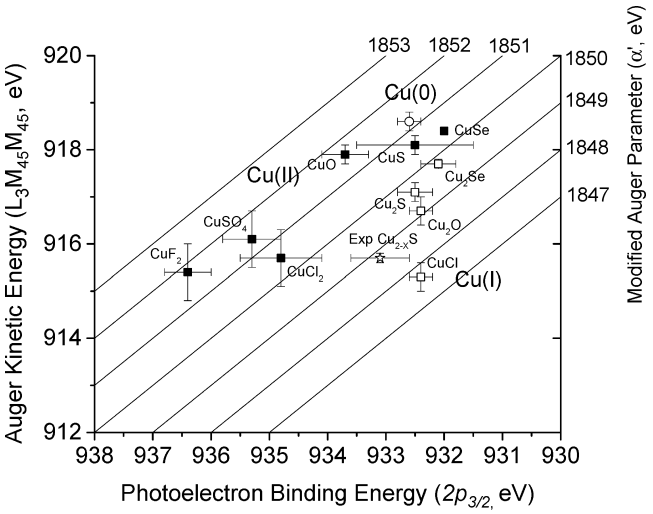

Figure 5. Wagner plot for Cu compounds compiled with data from the NIST database.[28] The empty circle is metallic copper or Cu(0); the filled squares are known Cu(II) compounds (labeled), and the empty squares are known Cu(I) compounds. "Exp $Cu_{2-X}S$" represents data for the nanoparticles deposited in pentacene.

The relatively low value for the modified Auger parameter makes clear the notably different chemical and electronic environments present in these $Cu_{2-X}S$ nanoparticles compared to the bulk species that have been thoroughly tabulated in the literature. The experimentally determined α' and Auger peak position found here were both lower than any of their respective values reported for bulk copper-containing com-

pounds (see Table 2). Mason et al. best conceptualized this effect by showing that the Auger kinetic energy values for small metal clusters were lower than for bulk copper-containing samples.[41−43] Specifically, an ∼3 eV decrease in the Auger kinetic energy for Cu(0) clusters compared to the bulk metal was attributed to both initial and final state effects that increasingly manifest themselves with a decreasing cluster size.[41,44,45] Initial state effects in this context are understood to be a change in the electronic structure of copper atoms in the cluster and are mainly attributed to a reduced electron density and result in a narrowing of the valence (3d) band. Although the effect is strongly dependent on the substrate, the major contribution of the final state effect is a result of a reduced relaxation energy. A change in the degree of atomic relaxation around the Cu(I) ion with regard to normal (bulk) Cu(I) compounds[37,39] is most likely caused by a reduced coordination around the copper atoms. The result is a weakened screening of the core hole produced by photoionization by both intra-atomic relaxation by electrons of the atom of interest and, more importantly, extra-atomic relaxation from neighboring atoms. These comparisons are relevant considering the low value for the Auger kinetic energy, which further supports the correlation with Cu(I) on the Wagner plot.

D. Sulfur Chemical State for $Cu_{2-X}S$ Nanoparticles in Pentacene. Table 2 and Figure 6a show the S 2p XPS core levels for $Cu_{2-X}S$ nanoparticles in pentacene, which indicate two distinct chemical environments for core and surface sulfur similar to that previously described for PbS nanoparticles.[23,26]

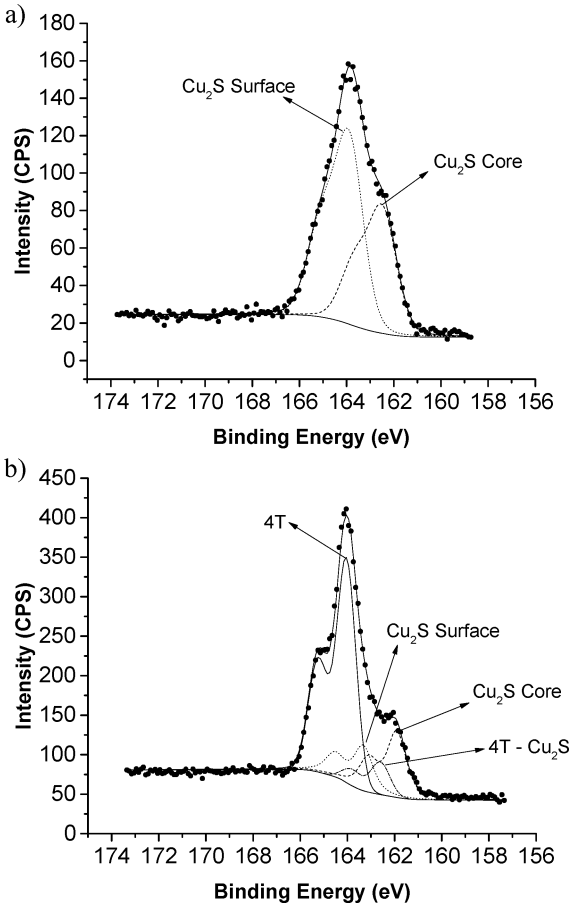

Figure 6. S 2p core level XPS of $Cu_{2-X}S$ deposited in (a) pentacene and (b) quaterthiophene (4T).

The binding energy of S $2p_{3/2\text{-CORE}}$ was 162.4 ± 0.2 eV, as shown in Figure 6 (where CORE refers to S within the center of the nanoparticle), which corresponds with the average value of 162.3 ± 1.7 eV for Cu_2S from the NIST database.[28] However, sulfur in CuS versus Cu_2S compounds cannot be distinguished by S 2p binding energy values alone as these overlap in the NIST database.

The surface component S $2p_{3/2\text{-SURF}}$ appeared at a higher binding energy, most likely because of unpassivated sulfur atoms on the $Cu_{2-X}S$ surface. A less likely explanation for the appearance of two separate sulfur species is that they arise from distinct S−S type bonding present at the surface, originating at corner atoms or other defect sites.[23,26,46,47] The S $2p_{3/2\text{-SURF}}$ binding energy was shifted higher by an average of 1.4 eV in both $Cu_{2-X}S$ films on C/Si and in $Cu_{2-X}S$ nanoparticles in pentacene, in agreement with the magnitude of "surface sulfur" component shifts seen for PbS and CdS nanocrystals.[46,47]

E. Chemical State of $Cu_{2-X}S$ Nanoparticles Deposited into Quaterthiophene. The survey scan of $Cu_{2-X}S$ codeposited into quaterthiophene was dominated by Cu, S, and C peaks (see the Supporting Information). The substrate was barely observable, with only low Si and O counts arising from the SiO_2 layer on the Si substrate.

All experimental data indicated $Cu_{2-X}S$ nanoparticles in quaterthiophene were Cu(I) and not Cu(II). The Cu 2p spectra (data not shown) did not display any of the secondary peaks or satellites expected for Cu(II). The peak positions of the Cu 2p and Auger $L_3M_{45}M_{45}$ peaks correlated with those in pentacene and would fall within the Cu(I) region in the Wagner plot shown in Figure 5 (data point not plotted).

The S 2p core level spectra of $Cu_{2-X}S$ codeposited into quaterthiophene are presented in Figure 6b. These S 2p spectra were deconvoluted into four major sources of sulfur, analogous to those observed previously for PbS nanoparticles in quaterthiophene.[23,26] These four sulfur components were assigned as arising from quaterthiophene at a binding energy of 164.1 eV (labeled 4T in Figure 6b), quaterthiophene interacting with the $Cu_{2-X}S$ nanoparticle at 162.7 eV (4T-Cu_2S), the surface component of $Cu_{2-X}S$ at 163.4 eV (Cu_2S Surface), and the core component of $Cu_{2-X}S$ at 162.0 eV (Cu_2S Core). No interference from the substrate was seen in the 2p spectra, and again, two peaks were required to fit the part of this sulfur spectrum arising from $Cu_{2-X}S$ nanoparticles.

IV. CONCLUSIONS

Cluster beam deposition was used to prepare ∼2.5 nm $Cu_{2-X}S$ nanoparticles in either pentacene or quaterthiophene that are free from the capping ligands usually required for colloidal preparation. These nanoparticles were determined to be nominally Cu_2S but are labeled as potentially copper-deficient because of the existence of several phases with similar stoichiometries.[13] Cluster beam deposition allowed direct control of nanoparticle stoichiometry and surface chemistry.[22,23] Pulsing the plasma discharge power increased process stability in the cluster beam deposition source and allowed $Cu_{2-X}S$ to be deposited without arcing. Together with thermal evaporation of organic matrices, cluster beam deposition can be used to grow nanoparticle films of a desired thickness and nanoparticle density that are free from the effects of oxidation and agglomeration that can arise during other preparation methods. The agreement between copper and sulfur XPS data indicated that similar $Cu_{2-X}S$ nanoparticles formed in both pentacene and quaterthiophene, as the matrix did not change

the nanoparticle morphology or chemical structure. Nevertheless, further studies are required to fully elucidate the local environment of Cu and S in the nanoparticles and to determine whether these nanoparticles are crystalline.

$Cu_{2-X}S$ nanoparticles with Cu(I) are better suited for light harvesting than the higher-band gap Cu(II) sulfide, and the former have been shown to be promising candidates for light-absorbing components for thin film and hybrid photovoltaic devices.[5,48−50] Thus, analysis of the nominal copper oxidation state was performed here to demonstrate that the thin film composition prepared here by cluster beam deposition might be well suited for use in photovoltaics. Specifically, XPS data indicated that only Cu(I) was present in the $Cu_{2-X}S$ nanoparticles, at least prior to atmospheric exposure. Prior work showed that Cu_2S nanoparticles prepared by different methods exhibit a direct band gap of 1.1−1.4 eV,[10] although the band gaps of these cluster beam-deposited films have not been experimentally verified. Furthermore, slightly copper-deficient $Cu_{2-X}S$ has also found recent application in plasmonic devices and nonlinear optics, including nanosensors, in part because of the p-doping and migration of Cu in the copper sulfide lattice giving rise to a local surface plasmon resonance.[8,10,51] Nevertheless, the ultimate utility of these $Cu_{2-X}S$−organic bulk-heterojunction films for photovoltaic application will be known only once they are evaluated electrically under simulated solar illumination. Such photoelectrical characterization of these films is now underway.

Finally, the use of chemical states or Wagner plots[33] was reprised here to determine the oxidation state of copper in these nanoparticles. These powerful yet relatively uncommon XPS data analysis strategies can also be applied to copper sulfide and other nanomaterials produced by other methods, making them worthy of further attention in the nanoscience community.

■ ASSOCIATED CONTENT

Supporting Information

Cluster beam deposition apparatus connected via high-vacuum load-lock to the X-ray photoelectron spectrometer, rate of deposition of $Cu_{2-X}S$ nanoparticles, additional XPS survey scans of deposited $Cu_{2-X}S$, Auger peak of deposited $Cu_{2-X}S$, S 2p region of $Cu_{2-X}S$, Si loss region on a bare Si wafer versus $Cu_{2-X}S$, and TEM of $Cu_{2-X}S$ nanoparticles in pentacene and quaterthiophene. This material is available free of charge via the Internet at http://pubs.acs.org.

■ AUTHOR INFORMATION

Corresponding Author

*E-mail: LHanley@uic.edu. Phone: (312) 996-0945.

Notes

The authors declare no competing financial interest.

■ ACKNOWLEDGMENTS

This work was supported by National Science Foundation Grant DMR-1206175.

■ REFERENCES

(1) Wadia, C.; Alivisatos, A. P.; Kammen, D. M. Materials Availability Expands the Opportunity for Large-Scale Photovoltaics Deployment. *Environ. Sci. Technol.* **2009**, *43*, 2072−2077.

(2) Kamat, P. V. Quantum Dot Solar Cells. Semiconductor Nanocrystals as Light Harvesters. *J. Phys. Chem. C* **2008**, *112*, 18737−18753.

(3) Hillhouse, H. W.; Beard, M. C. Solar Cells from Colloidal Nanocrystals: Fundamentals, Materials, Devices, and Economics. *Curr. Opin. Colloid Interface Sci.* **2009**, *14*, 245−259.

(4) Chandrasekaran, J.; Nithyaprakash, D.; Aijan, K. B.; Maruthamuthu, S.; Manoharan, D.; Kumar, S. Hybrid Solar Cell Based on Blending of Organic and Inorganic Materials: An Overview. *Renewable Sustainable Energy Rev.* **2011**, *15*, 1228−1238.

(5) Wu, Y.; Wadia, C.; Ma, W.; Sadtler, B.; Alivisatos, A. P. Synthesis and Photovoltaic Application of Copper(I) Sulfide Nanocrystals. *Nano Lett.* **2008**, *8*, 2551−2555.

(6) Deka, S.; Genovese, A.; Zhang, Y.; Miszta, K.; Bertoni, G.; Krahne, R.; Giannini, C.; Manna, L. Phosphine-Free Synthesis of P-Type Copper(I) Selenide Nanocrystals in Hot Coordinating Solvents. *J. Am. Chem. Soc.* **2010**, *132*, 8912−8914.

(7) Wang, Y.; Ai, X.; Miller, D.; Rice, P.; Topuria, T.; Krupp, L.; Kellock, A.; Song, Q. Two-Phase Microwave-Assisted Synthesis of Cu_2S Nanocrystals. *CrystEngComm* **2012**, *14*, 7560−7562.

(8) Liu, X.; Wang, X.; Zhou, B.; Law, W.-C.; Cartwright, A. N.; Swihart, M. T. Size-Controlled Synthesis of $Cu_{2-X}E$ (E = S, Se) Nanocrystals with Strong Tunable Near-Infrared Localized Surface Plasmon Resonance and High Conductivity in Thin Films. *Adv. Funct. Mater.* **2013**, *23*, 1256−1264.

(9) Wang, J.-J.; Xue, D.-J.; Guo, Y.-G.; Hu, J.-S.; Wan, L.-J. Bandgap Engineering of Monodispersed $Cu_{2-X}S_ySe_{1-Y}$ Nanocrystals through Chalcogen Ratio and Crystal Structure. *J. Am. Chem. Soc.* **2011**, *133*, 18558−18561.

(10) Zhao, Y.; Burda, C. Development of Plasmonic Semiconductor Nanomaterials with Copper Chalcogenides for a Future with Sustainable Energy Materials. *Energy Environ. Sci.* **2012**, *5*, 5564−5576.

(11) Okamoto, K.; Kawai, S. Electrical Conduction and Phase Transition of Copper Sulfides. *Jpn. J. Appl. Phys.* **1973**, *12*, 1130−1138.

(12) Riha, S. C.; Jin, S.; Baryshev, S. V.; Thimsen, E.; Wiederrecht, G. P.; Martinson, A. B. F. Stabilizing Cu_2S for Photovoltaics One Atomic Layer at a Time. *ACS Appl. Mater. Interfaces* **2013**, *5*, 10302−10309.

(13) Chakrabarti, D. J.; Laughlin, D. E. The Cu-S (Copper-Sulfur) System. *Bull. Alloy Phase Diagrams* **1983**, *4*, 254−271.

(14) Scharber, M. C.; Sariciftci, N. S. Efficiency of Bulk-Heterojunction Organic Solar Cells. *Prog. Polym. Sci.* **2013**, *38*, 1929−1940.

(15) Zhou, Y.; Eck, M.; Kruger, M. Bulk-Heterojunction Hybrid Solar Cells Based on Colloidal Nanocrystals and Conjugated Polymers. *Energy Environ. Sci.* **2010**, *3*, 1851−1864.

(16) Folmer, J. C. W.; Jellinek, F. The Valence of Copper in Suphides and Selenides: An X-ray Photoelectron Spectroscopy Study. *J. Less-Common Met.* **1980**, *76*, 153−162.

(17) Wang, L.; Li, D.; Hu, Y.; Jiang, C. Realization of Uniform Large-Area Pentacene Thin Film Transistor Arrays by Roller Vacuum Thermal Evaporation. *J. Vac. Sci. Technol., A* **2011**, *29*, 041510.

(18) Wilson, M. W. B.; Rao, A.; Ehrler, B.; Friend, R. H. Singlet Exciton Fission in Polycrystalline Pentacene: From Photophysics toward Devices. *Acc. Chem. Res.* **2013**, *46*, 1330−1338.

(19) Fichou, D.; Ziegler, C. In *Handbook of Oligo- and Polythiophenes*; Fichou, D., Ed.; Wiley-VCH: Weinheim, Germany, 1999; pp 185−282.

(20) Huisman, C. L.; Huijser, A.; Donker, H.; Schoonman, J.; Goossens, A. UV Polymerization of Oligothiophenes and Their Application in Nanostructured Heterojunction Solar Cells. *Macromolecules* **2004**, *37*, 5557−5564.

(21) Zachary, A. M.; Bolotin, I. L.; Hanley, L. In *Nanofabrication Using Focused Ion and Electron Beams: Principles and Applications*; Moshkalev, S., Ed.; Oxford University Press: New York, 2012; pp 457−485.

(22) Zachary, A. M.; Bolotin, I. L.; Asunskis, D. J.; Wroble, A. T.; Hanley, L. Cluster Beam Deposition of Lead Sulfide Nanocrystals into Organic Matrices. *ACS Appl. Mater. Interfaces* **2009**, *1*, 1770−1777.

(23) Pleticha, F. D.; Lee, D.; Sinnott, S. B.; Bolotin, I. L.; Majeski, M. W.; Hanley, L. Acetylene Ion-Enhanced Bonding of PbS Nanoparticles to Quaterthiophene in Thin Films. *J. Phys. Chem. C* **2012**, *116*, 21693−21698.

(24) Depla, D.; Mahieu, S.; Green, J. E. In *Handbook of Deposition Technologies for Films and Coatings: Science, Applications and Technology*; Martin, P. M., Ed.; Elsevier: Amsterdam, 2010; pp 253−296.
(25) Kelly, P. J.; Arnell, R. D. Magnetron Sputtering: A Review of Recent Developments and Applications. *Vacuum* **2000**, *56*, 159−172.
(26) Majeski, M. W.; Pleticha, F. D.; Bolotin, I. L.; Hanley, L.; Yilmaz, E.; Suzer, S. Photoresponse of Pbs Nanoparticle-Quaterthiophene Films Prepared by Gaseous Deposition as Probed by XPS. *J. Vac. Sci. Technol., A* **2012**, *30*, 04D109.
(27) Wijesundara, M. B. J.; Ji, Y.; Ni, B.; Sinnott, S. B.; Hanley, L. Quantifying the Effect of Polyatomic Ion Structure on Thin-Film Growth: Experiments and Molecular Dynamics Simulations. *J. Appl. Phys.* **2000**, *88*, 5004−5016.
(28) Naumkin, A. V.; Kraut-Vass, A.; Gaarenstroom, S. W.; Powell, C. J. In *NIST Standard Reference Database*, 20, version 4.1; National Institute of Standards and Technology: Gaithersburg, MD, (; http://srdata.nist.gov/xps/).
(29) Phillips, P. J.; Carnevale, S. D.; Kumar, R.; Myers, R. C.; Klie, R. F. Full-Scale Characterization of UVLED $Al_xGa_{1-x}N$ Nanowires Via Advanced Electron Microscopy. *ACS Nano* **2013**, *7*, 5045−5051.
(30) Sproul, W. D.; Christie, D. J.; Carter, D. C. Control of Reactive Sputtering Processes. *Thin Solid Films* **2005**, *491*, 1−17.
(31) Biesinger, M. C.; Lau, L. W. M.; Gerson, A. R.; Smart, R. S. C. Resolving Surface Chemical States in XPS Analysis of First Row Transition Metals, Oxides and Hydroxides: Sc, Ti, V, Cu and Zn. *Appl. Surf. Sci.* **2010**, *257*, 887−898.
(32) Goh, S. W.; Buckley, A. N.; Lamb, R. N. Copper(II) Sulfide? *Miner. Eng.* **2006**, *19*, 204−208.
(33) Moretti, G. Auger Parameter and Wagner Plot in the Characterization of Chemical States by X-ray Photoelectron Spectroscopy: A Review. *J. Electron Spectrosc. Relat. Phenom.* **1998**, *95*, 95−144.
(34) Pearce, C. I.; Pattrick, R. A. D.; Vaughan, D. J.; Henderson, C. M. B.; van der Laan, G. Copper Oxidation State in Chalcopyrite Mixed Cu D^9 and D^{10} Characteristics. *Geochim. Cosmochim. Acta* **2006**, *70*, 4635−4642.
(35) Iijima, Y.; Niimura, N.; Hiraoka, K. Prevention of the Reduction of CuO During X-ray Photoelectron Spectroscopy Analysis. *Surf. Interface Anal.* **1996**, *24*, 193−197.
(36) Chusuei, C. C.; Brookshier, M. A.; Goodman, D. W. Correlation of Relative X-ray Photoelectron Spectroscopy Shake-up Intensity with CuO Particle Size. *Langmuir* **1999**, *15*, 2806−2808.
(37) Kohler, M. A.; Curry-Hyde, H. E.; Hughes, A. E.; Sexton, B. A.; Cant, N. W. The Structure of Cu/SiO_2 Catalysts Prepared by the Ion-Exchange Technique. *J. Catal.* **1987**, *108*, 323−333.
(38) Satta, M.; Moretti, G. Auger Parameters and Wagner Plots. *J. Electron Spectrosc. Relat. Phenom.* **2010**, *178*−*179*, 123−127.
(39) Sexton, B. A.; Smith, T. D.; Sanders, J. V. Characterization of Copper-Exchanged Na-A, X, and Y Zeolites with X-ray Photoelectron Spectroscopy and Transmission Electron Microscopy. *J. Electron Spectrosc. Relat. Phenom.* **1985**, *35*, 27−43.
(40) Moulder, J. F.; Stickle, W. F.; Sobol, P. E.; Bomben, K. D. *Handbook of X-ray Photoelectron Spectroscopy*; Perkin-Elmer Corp.: Eden Prairie, MN, 1992.
(41) Mason, M. G. Electronic Structure of Supported Small Metal Clusters. *Phys. Rev. B* **1983**, *27*, 748−762.
(42) Shpiro, E. S.; Joyner, R. W.; Grunert, W.; Hayes, N. W.; Siddiqui, M. R. H.; Baeva, G. N. In *Zeolites and Related Microporous Materials: State of the Art 1994*; Weitkamp, H., Karge, H. G., Pfeifer, H., Holderich, W., Eds.; Elsevier Scientific B.V.: Amsterdam, 1994; pp 1483−1492.
(43) Gautier, M.; Durand, J. P.; Pham Van, L. Influence of the $Al_2O_3(0001)$ Surface Reconstruction on the Cu/Al_2O_3 Interface. *Surf. Sci. Lett.* **1991**, *249*, L327−L332.
(44) Nevolin, V. N.; Zenkevich, A. V.; Lai, X. C.; Pushkin, M. A.; Tronin, V. N.; Troyan, V. I. The Electronic States of Copper Clusters Pulsed Laser Deposited on Various Substrates. *Laser Phys.* **2001**, *11*, 824−836.
(45) Yang, D.-Q.; Sacher, E. Initial- and Final-State Effects on Metal Cluster/Substrate Interactions, as Determined by XPS: Copper Clusters on Dow Cyclotene and Highly Oriented Pyrolytic Graphite. *Appl. Surf. Sci.* **2002**, *195*, 187−195.
(46) Winkler, U.; Eich, D.; Chen, Z. H.; Fink, R.; Kulkarni, S. K.; Umbach, E. Detailed Investigation of CdS Nanoparticle Surfaces by High-Resolution Photoelectron Spectroscopy. *Chem. Phys. Lett.* **1999**, *306*, 95−102.
(47) Lobo, A.; Möller, T.; Nagel, M.; Borchert, H.; Hickey, S. G.; Weller, H. Photoelectron Spectroscopic Investigations of Chemical Bonding in Organically Stabilized PbS Nanocrystals. *J. Phys. Chem. B* **2005**, *109*, 17422−17428.
(48) Lee, H.; Yoon, S. W.; Kim, E. J.; Park, J. In-Situ Growth of Copper Sulfide Nanocrystals on Multiwalled Carbon Nanotubes and Their Application as Novel Solar Cell and Amperometric Glucose Sensor Materials. *Nano Lett.* **2007**, *7*, 778−784.
(49) Rivest, J. B.; Swisher, S. L.; Fong, L.-K.; Zheng, H.; Alivisatos, A. P. Assembled Monolayer Nanorod Heterojunctions. *ACS Nano* **2011**, *5*, 3811−3816.
(50) Liao, H.-C.; Tsao, C.-S.; Lin, T.-H.; Jao, M.-H.; Chuang, C.-M.; Chang, S.-Y.; Huang, Y.-C.; Shao, Y.-T.; Chen, C.-Y.; Su, C.-J.; Jeng, U. S.; Chen, Y.-F.; Su, W.-F. Nanoparticle-Tuned Self-Organization of a Bulk Heterojunction Hybrid Solar Cell with Enhanced Performance. *ACS Nano* **2012**, *6*, 1657−1666.
(51) Scotognella, F.; Valle, G. D.; Kandada, A. R. S.; Zavelani-Rossi, M.; Longhi, S.; Lanzani, G.; Tassone, F. Plasmonics in Heavily-Doped Semiconductor Nanocrystals. *Eur. Phys. J. B* **2013**, *86*, 154.